Controlled Engineering of Multifunctional Porous Structures Using Tri-needle Co-axial Electrohydrodynamic Flow and Sacrificial Media

Zhi-Cheng Yao[a], Chunchen Zhang[a], Zheng Xing[a], Zeeshan Ahmad[b], Qiuping Ding[a], Ming-Wei Chang[a,c*]

[a] College of Biomedical Engineering & Instrument Science, Zhejiang University, Hangzhou 310027, PR China

[b] The Leicester School of Pharmacy, De Montfort University, The Gateway, Leicester, LE1 9BH, UK

[c] Nanotechnology and Integrated Bioengineering Centre, University of Ulster, Jordanstown Campus, Newtownabbey, BT37 0QB, Northern Ireland, UK.

*corresponding author:

Dr. Ming-Wei Chang

Tel: +44 28 9536 7142
Email: m.chang@ulster.ac.uk

ABSTRACT

Three-dimensional porous architectures have gained popularity as advanced materials in emerging therapeutics, drug delivery systems and tissue regeneration. This is largely due to their porosity, inter-connectivity, and mechanical properties. However, current approaches to derive such three-dimensional structures are stochastic and therefore density uniformity varies, with innermost components exhibiting dense attributes. This also limits the encapsulation ability and quality of compounds. In this study, multifunctional structures comprising multi-layered particles are developed. Polycaprolactone (PCL)/ethyl cellulose (EC)/ ganoderma lucidum polysaccharide (GLP) is the outer layer; silicone oil (SO) is the intermediate layer; PCL and magnetic Fe_3O_4 nanoparticles (MNP) are the inner-most (core) component. Particles are initially formed using single step tri-needle co-axial electrostatic jetting, followed by sacrificial template removal to enable multifunctional porous structures. Using this approach, deployment of layered bodies enables the formation of homogeneous particles (150 μm) with tunable pore sizes of 100s of nanometers to 350s of microns. The process is versatile, and results indicate multi-scale pore size and hybrid pore connectivity are regulated through manipulation of the sacrificial agent. These structures are therefore promising for several multi-faceted healthcare applications e.g. targeted drug delivery, 3D cell culture, and real-time MRI imaging.

Key words: Porous; Triaxial Particle; Bioactive Encapsulation; Sacrificial Agents; MRI Imaging, Multi-scale.

1. Introduction

The role of porous architectures in advanced therapeutics and emerging bio-medical applications is constantly evolving based on key component integration and application derived design of such bodies [1-3]. Interconnected pore structure, large surface area, opportunistic pore size and low density of porous structures have been exploited to meet functional, structural or chemical needs of the end application [4, 5].

Several approaches exist to fabricate such structures and these include solvent casting [6], lyophilization [7], particle filtration [8], gas foaming [9] and phase separation [10]. Whilst these methods demonstrate opportunistic pathways in fabrication, challenges relating to polymer matrix isolation from the dispersion medium in consistent fashion remain. Extensive processing steps, elevated costs associated with material loss (phase transition) and limited process control for effective encapsulation of functional or bioactive entities throughout the 3D structure are common features which require further investigation. When engineering current methods yield less organised pore distribution, which present poor connectivity with a denser structure in the central zone, resulting abrupt change in microenvironment of the structure and further inhibiting cells penetration and migration [11, 12]. Therefore, porous structures with efficient pore size distribution and high specific surface area are required to improve cells activity. Additionally, these porous structures capable of encapsulation and protection of bioactive substances in a controlled fashion are desirable while such porous structures can serve as a platform for promoting real-time imaging of in-vitro/ in-vivo via a non-invasive imaging method. A cumulative delivery of different encapsulated bioactive and coherent imaging of structure location and interaction in the host environment can be improved for advanced applications.

The feasibility of engineering multilayer particles by deploying two immiscible fluids using co-axial electrohydrodynamic technology was first reported by Loscertales et al. in 2002 [13].

Since then, electrohydrodynamic technology making use of multiple-needles (>2) have been developed for various micro and nano-scaled structures such as core-shelled [14], hollow [15], janus [16], mono-porous [17], rope [18], multiple-inner cored[19], bubbles [20] and four-layered particles [21] for various applications in drug delivery, therapeutics and biomedical imaging. Moreover, Triaxial electrospray technique is a facile and versatile method to fabricate multi-layer spherical structures at ambient environment, which has been widely used to engineer particles ranging from tens of nanometers to hundreds of micrometers[22, 23]. The diameter and surface morphology of generated particles can be regulated by process parameters (e.g. flow rate, applied voltage and collector distance)[24, 25]. Particulate structures exhibiting multi-compartments have been loaded with a variety of drugs, including combinations where miscibility is often problematic. Furthermore, contrast agents for real-time imaging have also been embedded into such particles. The inherent nature of single-step elecrohydrodynamic atomisation (EHDA) engineering allows particulates to be deposited directly into a solvent which has been shown to be a cost-effective and convenient method of yielding porous polymeric structures[26, 27]. Here, selected sacrificial agents are removed post particle formation, resulting in hollow or void laden structures. Using EHDA, the inclusion of sacrificial agents at specific regions of multi-layered particles indicates a valuable pathway to engineer multi-scale porosity.

In this study, novel multi-scale (100 nm - 350 μm) porous structures, capable of integrating functional compounds (e.g. bioactive materials, API, image contrast agents etc.), are engineered. These provide opportunities for compartmentalised microparticles with simultaneous functions and roles, such as controlled release and magnetic resonance imaging (MRI). Solid microparticles comprising a core and two-layers were first made using tri-needle co-axial electrospray jetting. Resulting charged particles were treated electrostatic depositing and further removal of the sacrificial agents. This

resulted in a coalescence structure with multi-scale pore sizes (from nano-sclaed channels to macropores). Polycaprolactone (PCL) polymer was selected as the core and outer layer for multicompartment microparticles due to its good biodegradability, biocompatibility and excellent mechanical properties [28, 29]. Dimethyl silicone oil (SO) and ethyl cellulose (EC) were used as templating agents for multi-scale pore formation in intermediate and outer layers, respectively. Ganoderma lucidum polysaccharide (GLP) was selected as the bioactive agent in the outer-most layer and was selected based on its anti-cancer, immune-regulation, and anti-inflammatory bioactivity [30]. Magnetic iron tetroxide nanoparticles (MNP) were embedded into the inner-core matrix to enhance imaging contrast between engineered structure and its adjacent host environment (MRI positioning). The surface morphology, structure, chemical composition, mechanical properties and three-dimensional cell culture of fabricated films were studied *in vitro* alongside MRI imaging outputs and the release profile of the encapsulated GLP.

2. Materials and Methods

2.1. Materials

Polycaprolactone (PCL, M_w=4.5x10^3g/mol) was purchased from Sigma Aldrich (St. Louis Mo., USA). Dimethyl silicone oil (SO), magnetic iron tetroxide nanoparticles (MNP) (Fe_3O_4, mean diameter ~20 nm), ethyl cellulose, and Triton X-100 were obtained from Aladdin Chemistry Co., Ltd., Shanghai, China. Phosphate buffered saline (PBS), acetic acid (HAc), n-hexane, and hydrochloric acid (HCl) were obtained from Sinopharm Chemical Reagent Co., Ltd., Shanghai, China. Ganoderma lucidum polysaccharide (GLP) was supplied by Beijing Jingcheng Biotechnology Co., Ltd., Beijing, China. Agar was obtained from Shanghai EKEAR Bio&Tech Co., Ltd. Potassium ferrocyanide was purchased from Sangon Biotech Co., Ltd., Shanghai,

China. Rhodamine-phalloidin and 4',6-Diamidino-2-phenylindole (DAPI) dihydrochloride were supplied from Shanghai Yeasen Biotechnology Co., Ltd (Shanghai, China). Cells counting kit (CCK-8) was purchased from Dojindo Molecular Technologies, Inc. (Kumamoto, Japan). Milli-Q reference ultrapure water purifier (Molsheim, France) was used to produce ultrapure water. Modified Eagle's medium (MEM) and fetal bovine serum (FBS) were obtained from Invitrogen, CA., USA.

2.2. Fabrication of the Multi-scale Multifunctional Porous Structure

Layered microparticles were jetted *via* the electrospray process using a tri-needle co-axial device, as shown in Fig. 1. The apparatus comprised stainless-steel tri-needle, a high-power voltage supply (Glassman high voltage Inc. series FC, USA), three precision syringe pumps (KD Scientific KDS100, USA), and a metal ring connected to the ground electrode. For the tri-needle device, the inner and outer diameters of the inner needle were 0.5 mm and 0.31 mm, respectively. The intermediate needle possessed inner and outer diameters of 1.60 mm and 1.07 mm, respectively. The coarsest (and outermost needle) had inner and outer diameters of 2.85 mm and 2.26 mm, respectively. The tri-needle device was connected to the high voltage power supply and the metal ring was located directly below the needle assembly (5 mm). During the jetting process, spraying behaviour and modes were observed using a high-speed camera (Baummer TXG03C, Germany) to ensure stable-jetting modes were obtained; at which near-uniform microparticles are synthesised. Selected liquids were simultaneously infused (syringe pumps) into the tri-needle device. Each liquid was allocated an independent needle within the device and this also ensured the media was kept separate prior to merging at the needle exit. Firstly, a 20 w/v% PCL solution was initially prepared by dissolving the polymer into HAc. This was then supplemented with MNP at a concentration of 1 w/w%, and the resulting suspension was loaded into

a 5 mL plastic syringe. This was then infused (via silicone tubing) into the inner most needle of the tri-needle device at a constant flow rate of 1.6 mL/h. SO serving as one of the sacrificial components was loaded into a separate syringe and perfused into the intermediate needle at a flow rate of 3mL/h. For the outer layer, a mixture of PCL and EC at a weighted ratio of 3:1 was prepared. GLP (3.75 w/w%) was added to the resulting polymeric solution and was mixed further until a transparent solution was obtained. This was then perfused into the outer needle at a flow rate of 10 mL/h. An electric field was applied between the needle device and grounded metal ring. The distance between the needle and grounded metal ring was 5 mm, whilst the collector was 30 cm below the grounded metal ring.

Multi-layered microparticles were deposited on to an aluminium foil. In the first instance ethanol was used to remove EC in outer layer for 12 hrs. n-hexane was then used to remove SO from the intermediate layer for 2h. Finally, ethanol was re-used to draw out any remaining residual solvent in a chemical hood for 24 hours. Using identical parameters, a porous film structure fabricated from over-layering of deposited microparticles was achieved by extending the deposition time, as shown in Fig. 1b.

2.3. Morphology Assessment

Optical microscopy (OM, Pheonix BMC503-ICCF, China) was used to study the size distribution of engineered multi-layered microparticles. SEM was used to exam their surface morphology, dimension and porous structure or network. Prior to SEM imaging, samples were fixed on a metallic stub using double-side conductive tape and sputter coated. A thin layer of gold under vacuum was deposited on the samples surface for 90 seconds at a current intensity of 25 mA. SEM images were obtained using a field-emission scanning electron microscope (FEI Quanta 650 FEG; Hillsboro, OR) at an accelerating voltage of 20 kV. In order to assess cross-sectional SEM imaging of

structures, samples were folded into a multi-layer structure and fractured in liquid nitrogen.

2.4. Chemical Composition Detection

Fourier transform infrared (FTIR) spectroscopy was used to analyze the sample composition. Sample pellets were prepared by mixing 2 mg of engineered structures with 200 mg KBr powder by grinding and subsequently compressing the mixture into transparent pellets under a pressure of 12 MPa. The pellets were then scanned (IR, Affinity 1, Shinadzu, Japan). Spectra were obtained at a resolution of 4 cm^{-1} ranging from 4000 to 500 cm^{-1}. Each spectrum was obtained using 10 scans. X-ray diffraction (XRD) was afforded with a diffractometer (X'Pert PRO; PANalytical, the Netherlands) associated with a standard Cu Kα radiation source ($\lambda = 1.5405$Å) and scanned within a 2θ range of 5-80° at a step size of 0.026°. The operating voltage and current were 40 kV and 40 mA, respectively.

2.5. Porous Structure Measurement

An automated mercury porosimeter (AutoPore IV 9510, Micromeritics Inc., USA) was used to measure porosity and pore size of samples. Surface tension and contact angle of mercury were 485 dynes/cm and 130°, respectively. Samples were dried in vacuum desiccator for 24 hours. Test range of pressure was 0.10 -60,000 psia.

2.6. Surface Water Contact Angle

Hydrophobicity/hydrophilicity of composite porous membranes was assessed through water contact angle (WCA) measurements using an optical contact meter (SL200KB, KINO Industry Co. Ltd., USA). Samples with thickness of 40±5 μm and 200±15 μm were obtained by depositing particles for 2 and 8 hours, respectively. Sacrificial agents were removed, and samples were dried. Measurements were performed using a three-axis horizontal tilt stage and observed in the sessile drop mode at 25 ℃. A 10 μL water

droplet was dripped onto each sample. The mean value of left and right WCAs on each sample was simulated using Young-Laplace fitting method and recorded [31].

2.7. Mechanical Test

Tensile tests were performed using a universal materials tester (Zwick/Roell Z020, Zwick, Germany). The selected gauge length was 10 mm, and samples were extended along the vertical direction with a 500 N load cell at a crosshead speed of 10 mm/min at the ambient temperature (25 ℃). Here, test structure sample was disposed into dimensions of 75×4 mm^2. For each sample set, measurements were taken in triplicate, and the mean tensile strength was calculated.

2.8. Magnetism and MRI Tracing Effect

To explore the magnetism of the porous structure, magnetization curve of samples was monitored using vibration sample magnetometer (Versalab, Quantum Design, Inc., San Diego, USA) at 300 K under magnetic field strengths between -10,000 and 10, 000 Oe. To evaluate contrast capability of engineered structures, MRI images were obtained from a 3T MRI system (Magnetom Prisma, Siemens Healthcare, Erlangen, Germany). Porous structures with 1 w/w% MNP were embedded in agarose phantom to mimic an *in-vivo* environment. Samples were placed into the head/neck coil region with 20 channels. For preparing agarose phantom, 1-gram agar was mixed with 100 mL DI water, and then heated to 100 ℃ and cooled down to 45 ℃. This temperature cycling was carried out several times to achieve a homogeneous agar gel. All phantoms to be used for MRI were then prepared by mixing samples with 10 mL of the pre-prepared agar gel and 2 mL of 5% w/v SDS aqueous solution to improve sample wetting and enhance phantom uniformity. Sample gel mixtures were stirred thoroughly to form a uniform suspension, which was then poured into a 15 mL centrifuge tube before MRI imaging. Pure agar phantoms without samples were fabricated as control groups.

T1-weighted images were obtained using a spin-echo (SE) sequence (TR/TE=2300 ms/2.38 ms, FOV=192×192 mm^2, slice thickness=1 mm). T2-weighted imaging were performed using the multi-TE SE sequence (TR/TE=5000 ms/393 ms; FOV=192×192 mm^2; FA=180°; matrix size=256×256; slice thickness=1 mm; bandwidth=781 Hz/Px).

2.9. Bioactive Release Profile

Standard curve of GLP in PBS was determined by measuring a series of absorbance of GLP solutions with different concentrations at 221 nm (the characteristic UV-Vis absorption of GLP) using a UV-2600 spectrophotometer (Shimadzu, Japan).

For measuring the loading capacity (LC) and encapsulation efficiency (EE) of GLP in the porous structure. 100 mg samples were fully dissolved in 10 mL HAc. After centrifuging, the solid residuals were transferred into 10 mL PBS for further dissolution. 4 mL supernatant was employed for measuring the absorbance. LC and EE were determined using Equations (1) and (2) [32, 33]:

$$LC\ (\%) = \frac{Amount\ of\ GLP\ content\ entrapped\ in\ \ the\ scaffolds\ (mg)}{Weight\ of\ scaffold\ sample\ (mg)} \times 100\% \quad (1)$$

$$EE\ (\%) = \frac{Amount\ of\ GLP\ content\ entrapped\ in\ \ the\ scaffolds\ (mg)}{Theoretical\ total\ amout\ of\ GLP\ added\ into\ the\ scaffolds\ (mg)} \times 100\% \quad (2)$$

For figuring out *in-vitro* release profile of the porous structure, 100 mg of samples were placed into 10 mL PBS and incubated at 37 ℃. At predesigned time intervals, 4 mL of supernatant was removed from the assessment medium and replaced with 4 mL of fresh test medium. The supernatant was filtered with a 0.45 μm Millipore filter, and assessed using UV-Vis analysis. The percentage of GLP release was calculated using Equation (3) [34]:

$$GLP\ release\ (\%) = \frac{Q_t}{Q_s} \times 100\% \quad (3)$$

Where, Q_t is the quantity of GLP release at time t, Q_s is the total quantity released.

To expand on diffusivity of GLP from the porous structure, we utilized the Korsmeyer-Peppas model to evaluate in-vitro release kinetics, which is expressed as shown in Eq. (4) [19]:

$$\frac{M_t}{M_\infty} = kt^n \quad (4)$$

Here, M_t and M_∞ indicate the percentage of drug released at time t and infinite time ∞, respectively. The k value is a characteristic constant, when n is the release exponent. A release exponent value below 0.45 represents Fickian diffusion or case-I diffusion, while an n value greater than 0.85, indicates case-II diffusion, which indicates certain interactions existing among drug molecules, release medium and the delivery matrix. When n value is in the range of 0.45-0.85, an anomalous transport process is proposed, which involves multiple factors contributing towards the release mechanism[35].

2.10. Cytotoxicity Test

Cell counting kit (CCK-8) was used to assess cytotoxicity of the structure. L929 cells were incubated and maintained in MEM medium supplied with 10 % FBS at 37℃ in 5% CO_2. The porous sample was trimmed into equal quality sterilized under UV for 2 hours. 100 µL of L929 cells suspension were seeded in a 96-well plate at a density of 1.5×10^4 cells/well and incubated for 24 hours. At 10, 24, 72, and 120 hours during cell culture, CCK-8 was set to evaluate the viability of L929 cells. By adding 20 µL CCK-8 solution to each well and incubating for further 3 hours, absorbance was measured at a wavelength of 450 nm using a microplate reader (Multiskan GO, ThermoFisher Scientific, USA). Cells viability in polystyrene well plate was used as a control and the culture medium with CCK-8 solution was utilized as a blank. The relative cell viability was calculated as Equation (5) [36]:

$$Cell\ viability\ (\%) = \frac{Absorbance\ (sample) - Absorbance\ (blank)}{Absorbance\ (control) - Absorbance\ (blank)} \times 100\% \quad (5)$$

2.11. Three-dimensional Cells Culture

Samples were trimmed into the same size (2 cm×2 cm) and immersed in ethanol for 4 hours to be sterilized. After being dried out in chemical hood, 1 mg/mL of porous structure was placed in petri dish. Cells grew on both of the upper and lower surfaces of the structure were evaluated. After co-culturing L929 cells with the samples for 3, 5, and 10 days, cells were fixed using 4 v/v% formalin for 15 min at ambient temperature, and then washed using PBS. Cells were then permeabilized with 0.1% Triton X-100 for 10 min. The cell cytoskeleton and nuclei were stained with phalloidin and DAPI for 1 min and 5 min, successively, and then washed with PBS. An inverted fluorescence microscope (Nikon Ti-S, Japan) was recruited to observe the cells morphology. A confocal microscope (Nikon C2 Plus, Japan) was further employed to detect the cells distribution on three-dimension in the porous structure. Also, in order to compare top and bottom surface of the porous structure, cell growth behavior was test on both two surfaces, with turning the lower surface up when using it to coculture with cells. In addition, a 30^{o} tilting angle was set up to mimic the un-horizontal in-vivo direction of cells migration. In the control group, no material was added to incubate the cells.

2.12. Statistical analysis

All experiments were carried out in triplicate and the data is presented as mean±standard deviation (n=3). Statistical analysis was implemented using SPSS software (SPSS Statistic v 18, IBM, UK) and the significant differences between variables were tested via one-way analysis of variance (ANOVA) followed by student's t-Test.

3. Results and Discussion

3.1. Preparation of multi-scale porous structure

At coflowing conditions, with the application of an electric field between the nozzle and collector, four jetting modes arise: dripping mode, coning mode, stable cone-jet mode, and multi-jetting mode [37]. Microparticles were prepared using a tri-needle co-axial jetting process combined with a templating approach to obtain multi-layered particles (using PCL as the inner core and outer shell with silicone oil as a middle layer). Pure ethanol was used to remove the mixed EC whilst the silicone oil was removed using n-hexane (Fig. 1b). Further to this, pure ethanol was used to wash out the residual solvents. Fig. 1c shows the preparation of the porous structures. The architecture was achieved by depositing microparticles on aluminium foil, followed by the removal of sacrificial agents using ethanol and n-hexane as described above. Porous structures were obtained after drying in a chemical hood.

The morphology of the particles before and after templating treatment are shown in Fig. S1. As indicated in Fig. S1, the tri-needle co-axial particles which were formed fell in a size range of 146.8 μm with a size distribution of 35.0 μm. It was found that the particles possessed a solid spherical structure before treatment was applied (Fig. S1a). However, the tri-needle co-axial particles that possessed a smooth surface were converted into narrow channels which can be observed on the surface layer (indicated with the white arrows in Fig. S1b) after removing the EC on the outer layer and the middle oil layer (SO).

Furthermore, the SEM images established that the spherical structure had collapsed into flatten morphology after removing the sacrificial agents (Figs. S1c-d), demonstrating that EC and SO were removed from the particles in the process. This result confirms the ability to remove a middle layer (in this case, SO) of a tri-needle co-axial jetted particle.

Porous structures were fabricated by continuously jetting the tri-needle co-axial particles. After deposition of the formulation for 2 hours, the inner and surface structure morphology of the produced porous particles are presented as shown in Fig. 2. Optical micrograph images presented structures which consisted of particles with uniform diameter distribution, as well as the adhesive periphery among the particles (Figs. 2a-b). After removing the sacrificial agents in the middle layer (SO) and outer layer (EC), a clear hierarchy between the adjacent particles and clearer image of the structure can be observed (Figs. 2c-d). Due to the removal of the surficial agents, more optical light passed through the porous structure, resulting in a more enhanced image.

Figs. 2e shows a cross-sectional SEM image of the structure obtained via jetted tri-needle co-axial particles before the removal of the sacrificial agents. These structures are compact and solid without channels or pores as shown in the high magnification SEM (Fig. 2f). The particles were insufficiently desiccated before being deposited on the collector, which further results in the inter-coalesce and tangent of the particles (Fig. 1C). It should be noted that solvent evaporation begins at the polymer-liquid interface which then penetrates through the self-infiltration of multi-layered polymers. For soft deformable particles, the drying process induces capillary-driven packing, resulting in a higher densification than in non-deformable analogues. Furthermore, the capillary pressure gradient allows particles to pass through the gaps formed in jetted structures [38]. For this phenomenon to occur, the particles need to be assembled and coalesced before drying occurs. At the interfacial boundary of the particles, the density and viscosity of weighted average mixture, based on the distribution of the liquid volume fraction, can be described as [39]:

$\rho = \alpha\rho_l + (1-\alpha)\rho_s$ and $\mu = \alpha\mu_l + (1-\alpha)\mu_s$, respectively.

The subscripts *l* and *s* denote the liquid and solid phases, correspondingly.

This equation predicts the particle assembly by undried particles between and further into the channels of textured structure. With further solvent evaporation, particles ultimately accumulated, while solidification of the particles move through created gaps. However, after removing the sacrificial agents, the thickness of the structures obtained had decreased from 152.0±14.6 μm to 74.9±15.4 μm (Fig. 2g), with two kinds of porous structures appearing (Fig. 2h), a nano-porous outer shell and microporous inner core with an interconnected pore structure. During the removal of the sacrificial agents, larger pores were obtained through the removal of the SO from the middle layer, whilst smaller pores presented in a random distribution, as a result of washing out the EC in the outer layer. This heat-free pore formation provides minimum consequences to the underlying pore features. However, a solidified interface is formed between the solidification zone and the non-coagulation zone of the particle, moving slowly from the outer layer to the core. Therefore, it can be established that the solidification shrinkage of the particle results in a thinner structure. Furthermore, an uneven topography with micropores present was observed on the upper surface of the structure (Figs. 2i, 2j), while a smoother topography with dipped cavities about 70 μm in size was presented on the lower surface (Figs. 2k and 2l). Such micropores on the lower surface might be formed in the process of detaching the films from the aluminium foil collector. However, a porous network of polymeric interconnects can be identified, allowing efficient fluid diffusion whist offering consistent assembly even on uneven substrates.

3.2. Chemical component analysis

Multiple excipients (PCL, GLP, MNP, SO, and EC) were utilized to produce the composite microparticles in a one-step tri-needle co-axial jetting process before creating porous structures. To investigate characteristics in material composition before

and after the treatment, FTIR was used to analyse the chemical components present in the material. The characteristic peaks of the components (before removing EC and SO) and the porous structure (after removing EC and SO) were compared. Feasibility of sufficiently washing out the sacrificial agents was also evaluated.

Fig. 3a shows FTIR of tri-needle co-axial jetted structures before and after removing the sacrificial agents. Characteristic peaks of SO appear at 1257 cm^{-1}, 1094 cm^{-1}, 1023 cm^{-1}, 798 cm^{-1} [28]; characteristic peaks of EC appear at 3442 cm^{-1}, and 2862 cm^{-1} [40]. The presence of MNP is presented by the peak at 1551 cm^{-1} [37]. Components of GLP are detected at 1035 and 1079 cm^{-1}, corresponding to the C-N stretching of amine groups within polysaccharide [10]. The FTIR spectrum of the porous structure shows that after the removal of the sacrificial agents, the porous structure did not show any characteristic peaks of SO or EC, demonstrating that the sacrificial agents were effectively removed to form a porous structure in the process.

Furthermore, the XRD spectra of the porous structure (Fig. 3b) presents the same diffraction peaks as PCL at the 2θ value of 21.4° and 23.8°, demonstrating that PCL exists in a crystal structures [41]. The flat curve in the range of 5° to 30° demonstrates the amorphous structure of GLP [37]. Characteristic peaks of XRD spectrum at 30.1^{o}, 35.5^{o}, 43.2^{o}, 57.0^{o} and 62.6^{o} confirm the appearance of MNPs [41]. These results further confirm that the sacrificial agents, SO and EC, were efficiently washed out, while the bioactive reagent (GLP) was not affected.

3.3. Physical properties of the porous structure

Fig. 4a shows that the porosity of the structure measured at 78.85 % by using a mercury porosimeter with a performance density of 0.76 g/mL according to literature [42]. The pore size of the porous structure fell in a range of 100 nm to 357 μm, while two of the

main pore sizes were observed at 1 μm and 100 μm, as a result of the removal of the EC on the outer layer and the SO in the middle layer.

Surface hydrophilicity is another important factor which can significantly affect cell growth, adhesion and proliferation on the porous structure [43]. Therefore, in this study, surface water contact angle was used to characterize the surface hydrophilic property. Contact angles of porous structure with different film thickness (Film-40: 40±5 μm; Film-200: 200±15μm) were recorded in a 1-hour time interval. As shown in Fig. 4b, the contact angles of Film-40 and Film-200 were hydrophilic initially 54.7±2.8° and 65.9±2.4°, respectively. Thicker films produced by extending the deposition time exhibited less hydrophilic characteristics. The thicker film exhibited more hydrophobic property due to higher surface roughness and inner voids during longer time for particles deposition [44]. However, the contact angle decreased on both films as time increased. For the Film-40, the angle disappeared at 45 minutes, while for the Film-200, it decreased to 20.2±3.3°, and then disappeared at 1 hour. The early disappearance of the contact angle in case of the Film-40 was due to the enhanced capillary force on the surface compared to the Film-200 [45]. This result demonstrates the surface hydrophilic property of the porous structure. Also, it reconfirms the inner porous interconnectivity of the structure, allowing the water droplet to transmit faster from the outer surface into the inner area of the structure.

Suitable mechanical properties are another key factor for porous structures, allowing sufficient temporary mechanical support to sustain different applications. Therefore, in order to investigate the mechanical properties, when preparing such porous structures via the removal of sacrificial agents, structure samples was disposed into dimensions of 75×4 mm^2. As shown in Fig. 4c, the Young's modulus of the porous structure is 257.0±41.3 MPa, with a breaking stress of 5.5±1.46 MPa, and an elongation of 5.0±0.2

%. The results demonstrate the mechanical properties of the structure to be consistent, proving the feasibility and repeatability of using this technique to prepare porous structures in the future. Most of the applied stress during the tensile strength test was applied to the PCL porous structures and the contact interface between the PCL structures [46]. The modulus of the structure was improved by manipulating the porous structure within an appropriate range, since the modulus is related to the porosity (Φ) of the materials following a condition of $E=E_0 \times (1-\Phi^{2/3})$, where E_0 is the Young's modulus of the compact materials without pores [46, 47]. Therefore, even with the high porosity of the porous structure, stronger mechanical properties were achieved by the present method which can be observed when compared to other porous structures made from PCL [46].

3.4. In-vitro magnetic properties and MRI evaluation

Fig. 5a shows the hysteresis loops of the magnetic porous structure prepared via depositing the tri-needle co-axial particles, the corresponding saturation magnetization values was 0.05 emu/g. Hysteresis loops show negligible coercivity and remanence magnetization, indicating that Fe_3O_4 nanoparticles were well dispersed in the structure via tri-needle co-axial jetting. Further, the ferric iron was stained with Prussian-blue (shown in inset Fig 5a), allowing the potassium ferrocyanide to combine with the ferric iron and therefore forming the ferric ferrocyanide [48]. The porous structure appeared uniformly blue, demonstrating the homogeneously distribution of Fe_3O_4 in the porous structure without any aggregation since Fe_3O_4 NMPs were encapsulated in the multi-layered particles before forming porous structure.

To evaluate the structure formed, MRI imaging was used. Magnetic properties of the structure were further confirmed by applying a strong magnetic field to vials hosting

the samples with various macro structures. Samples were incised, folded or wrapped into different shapes, loose pack structure (A), dense pack structure (B), solid cylinder structure (C), hollow tube-like structure (D), and folding fan structure (E), following with embedded different samples into agarose phantoms (Figs. 5b). Samples were fabricated and both quantitative T_1 and T_2 MRI mappings were explored. Furthermore, T_1- and T_2-weighted MRI images were analysed as shown in Figs. 5c and 5d, respectively. Both images show clear boundaries of the samples, indicating that the microstructural variation of the porous magnetic structure can be monitored by MRI after being implanted in-vivo. The results show that the magnetic porous structure has potential as contrast agents for both T_1 and T_2 MRI imaging experiments. Additionally, comparing the T_1- and T_2-weighted MRI images, clearer boundaries of the samples were detected under T_2-weighted imaging. This is due to the Fe_3O_4 nanoparticles reducing the T_2 relaxation time, which is more notable than the impact on T_1, and further enhancing the contrast between the structure and agarose phantom in T_2-weighted gray image [37].

3.5. Bioactive release profile measurement

Using GLP as a bioactive loaded model to evaluate release profile of the composite porous structure. GLP was loaded in the outer layer of the tri-needle co-axial microparticles, which were subsequently to from porous structure. It was found that the loading capacity and encapsulation efficiency of GLP were 3.72±0.07 % and 94.32±1.85 %, respectively. As shown in Fig. 6a, the releasing profile can be divided into three stages: initial burst release stage from 0 to 15 minutes with cumulative release percent reaching 73.68 %; the second stage is fast release from 15 minutes to 4 hours with cumulative release percent reaching 82.09 %; Finally, it is the slow release process from 4 hours to 120 hours, with cumulative release percent achieving 85.07 %. Quick

release of the GLP is mainly caused by the water solubility of GLP [43] and transability through pore connectivity of the porous structures facilitating the release dynamic. It is noteworthy that although permeability and diffusivity of generated structures using quantified fluid or air flow through porous media is valuable [49], the Korsmeyer-Peppas model was used to fit the release curve to evaluate in-vitro release mechanism and release rate from the generated matrix. For the Korsmeyer-Peppas model fitting shown in Table 1, the n value for the present study is 0.04, indicating GLP release from porous structures is via Fickian diffusion. Variations to the k value suggests structures could be engineered to tailor drug release. Hence, loading of GLP into the porous structures in a single step must be optimized to ensure drug release is appropriate, where the release of active is sufficient to inhibit and further reduce bacterial infection over a designated time period.

Table 1. Fitting parameters of GLP release from the porous structure.

Korsmeyer-Peppas model		
R^2	k	N
0.98	77.45	0.04

At post-release at 120 hours, the structures were dehydrated as observed under SEM. The surface morphology of the upper and lower surfaces of the structures after GLP release have not much changed as shown in Figs. 6b-g. The humps emerged on the upper surface of the structure while on the lower surface rounded pores with an average diameter of 1 μm appeared (Fig. 6g), which may be due to the dissolution of GLP in PBS.

3.6. In-vitro cell culture and biocompatibility

To evaluate cytotoxicity of the tri-needle co-axial jetted porous structure, L929 cells were co-cultured with the structure for different time periods (10, 24, 72, and 120 hours).

It was found that with an increase in time, the viability of the cells slightly decreased as shown in Fig. S2. Cells viability was 90.82±5.10 % after 24 hours of incubation, whilst at 120 hours it decreased to 86.84±11.36 %. A decrease in cell viability might be the result of the effect of the structure on reducing cell attachment to the bottom of the plates, which further led to a decrease in cell growth and proliferation. However, these results demonstrate that the structure was not cytotoxic [32].

3.7. Cells migration in 3D culture environment

The In-vitro experiments in testing cells growth on both upper and lower surfaces of the structures were explored considering the three-dimensional environment. After 3, 5, and 10 days of culture, cell morphology on the upper surface of structures were presented in Fig. 7. Cell growth behaviour has reconfirmed the biocompatibility of the structures. It appears that the cells not only adhered to the structure surface, but also penetrated into the structure through the pores on the surface during days 3 and 5. After 10 days of culture, the coverage of the cells on the structure surface had increased. Furthermore, the cells also filled in the pores on the lower surface of the structure (bottom 2 rows in Fig. 7).

Compared to the lower surface, the upper surface of the structure shows more obvious uneven topography, cells tended to migrate into the inner zone of the structure passing through the channels and pores on the surface, and then proliferate. However, the lower surface presents a smoother and denser structure, improving cell adhesion, while inhibiting migration of cells into the film. After a 10-day incubation, it was observed that there were still a great number of cells on the lower surface instead of migrating into the inner of the structure (the bottom row in Fig. 7).

To simulate the tilted environment of the material application, L929 cells with and without porous sample were incubated in tilting petri dishes at 30° for 3 days. As shown

in Fig. 8, cells grow and proliferate as normal in the tilted petri dishes (top 2 rows in Fig. 8). However, cell growth on the tilted sample surface can be observed, while most of the cells migrated to the inner zone of the structure (bottom 2 rows in Fig. 8), presenting randomly spreading direction. This result demonstrates that the structure provides an optimal environment for cells 3D culture. Cell growth mainly depends on the pore connectivity of the structure, whilst the tilt angle did not affect the cell behaviour.

Confocal microscope was further employed to detect the cell distribution in three-dimension in the porous structure. After culturing with the structure for 3, 5, and 10 days, cell distribution was presented in Fig. 9, where the indicating colour reflects the depth of the cell location in the structure. It appears that for the controlled group, the cell number increased with an increase in culture period. However, when incubated with the porous structure, and extending the culture period, the cell number also increased with cells spreading over a wider area of the inner zone of the structure.

Fig. 9b shows the cells distributed in a thickness range of 150 μm after a 10-day culture. It was confirmed that with increasing culture period in the porous structure the cells distribution range increased as shown in the location at xy, xz, and yz orientations. At post-culture 10 days, cells appeared in a two-layer distribution, with a higher cell number on the lower surface than the upper one. This was due to cell penetration from the surface to the inner zone of the engineered structures, which led to non-uniform cell distribution on both upper and lower surfaces of resulting structures [50, 51]. However, in the culture dish, the cell distribution appeared no obvious difference in the 10-day culture period. This result demonstrates the facilitation of the porous structure on cells migration in a 3D culture environment. This unique 3D structure has potential for anti-biofilm applications to provide optimal cargo system for sustained drug release to ensure long-term antibacterial

protection of biomedical devices as encapsulated polysaccharide enables strong antibacterial activity against common pathogens [52-54].

4. Conclusion

A novel multifunctional porous structure possessing hybrid pore connectivity and distribution was fabricated using tri-needle co-axial jetting. Multilayered spherical particles were successfully engineered hosting a sacrificial agent which was subsequently removed. Crosslinking of jetted tri-needle co-axial particles provides structural integrity which enabled uniform distribution of both encapsulated bioactive and imaging contrast agents. The process gives rise to homogeneous particles (150 μm) with tunable pore sizes of 100s of nanometers to 100s of microns. This facilitates real-time MRI imaging; making use of porous structure location and interaction between host environments under T_1- and T_2-weighted images. One standout feature is porous structures with well-defined macro- and nano-scaled pores significantly increase efficiency of 3D cell culture, where smaller pores allow bioactive transmission, and larger pores improve cell growth in the central zone. The proposed mechanism also enables the construction of porous structures with homogeneous encapsulation and localization of molecules without hydrophilicity or lipophilicity constraints. This is due to the state-of-the-art synthesis approach in the production of multifunctional porous structures.

Conflicts of interest

There are no conflicts of interest to declare.

Acknowledgement

This work was financially supported by the National Natural Science Foundation of China (No. 81771960), the Key Science Technologies R&D Program of Zhejiang Province (2015C02035), and the Fundamental Research Funds for the Central Universities (2017QNA5017).

References

[1] J. Zhao, C.-S. Liu, Y. Yuan, X.-Y. Tao, X.-Q. Shan, Y. Sheng, F. Wu, Preparation of hemoglobin-loaded nano-sized particles with porous structure as oxygen carriers, Biomaterials 28 (2007) 1414-1422.

[2] N. Jayaprakash, J. Shen, S.S. Moganty, A. Corona, L.A. Archer, Porous hollow carbon@ sulfur composites for high-power lithium–sulfur batteries, Angewandte Chemie International Edition 50 (2011) 5904-5908.

[3] D.A. Edwards, J. Hanes, G. Caponetti, J. Hrkach, A. Ben-Jebria, M.L. Eskew, J. Mintzes, D. Deaver, N. Lotan, R. Langer, Large porous particles for pulmonary drug delivery, Science 276 (1997) 1868-1872.

[4] E. Tasciotti, X. Liu, R. Bhavane, K. Plant, A.D. Leonard, B.K. Price, M.M.-C. Cheng, P. Decuzzi, J.M. Tour, F. Robertson, Mesoporous silicon particles as a multistage delivery system for imaging and therapeutic applications, Nature nanotechnology 3 (2008) 151.

[5] J. Liu, A. Stace-Naughton, X. Jiang, C.J. Brinker, Porous nanoparticle supported lipid bilayers (protocells) as delivery vehicles, Journal of the American Chemical Society 131 (2009) 1354-1355.

[6] S. Taherkhani, F. Moztarzadeh, Fabrication of a poly (ε-caprolactone)/starch nanocomposite scaffold with a solvent-casting/salt-leaching technique for bone tissue engineering applications, Journal of Applied Polymer Science 133 (2016).

[7] H. Xia, D. Zhao, H. Zhu, Y. Hua, K. Xiao, Y. Xu, Y. Liu, W. Chen, Y. Liu, W. Zhang, Lyophilized scaffolds fabricated from 3D-printed photocurable natural hydrogel for cartilage regeneration, ACS applied materials & interfaces 10 (2018) 31704-31715.

[8] T.D.H. Le, V. Liaudanskaya, W. Bonani, C. Migliaresi, A. Motta, Enhancing bioactive properties of silk fibroin with diatom particles for bone tissue engineering applications, Journal of tissue engineering and regenerative medicine 12 (2018) 89-97.

[9] S.A. Poursamar, J. Hatami, A.N. Lehner, C.L. da Silva, F.C. Ferreira, A.P.M. Antunes, Gelatin porous scaffolds fabricated using a modified gas foaming technique: Characterisation and cytotoxicity assessment, Materials Science and engineering: C 48 (2015) 63-70.

[10] Z.-C. Yao, C. Zhang, Z. Ahmad, J. Huang, J.-S. Li, M.-W. Chang, Designer fibers from 2D to 3D–Simultaneous and controlled engineering of morphology, shape and size, Chemical Engineering Journal 334 (2018) 89-98.

[11] A. Petersen, A. Princ, G. Korus, A. Ellinghaus, H. Leemhuis, A. Herrera, A. Klaumünzer, S. Schreivogel, A. Woloszyk, K. Schmidt-Bleek, A biomaterial with a channel-like pore architecture induces endochondral healing of bone defects, Nature communications 9 (2018) 1-16.

[12] F. Qu, J.L. Holloway, J.L. Esterhai, J.A. Burdick, R.L. Mauck, Programmed biomolecule delivery to enable and direct cell migration for connective tissue repair, Nature communications 8 (2017) 1-11.

[13] I.G. Loscertales, A. Barrero, I. Guerrero, R. Cortijo, M. Marquez, A.M. Ganan-Calvo, Micro/nano encapsutation via electrified coaxial liquid jets, Science 295 (2002) 1695-1698.

[14] M. Chang, M. Edirisinghe, E. Stride, Ultrasound mediated release from stimuli-responsive core–shell capsules, Journal of Materials Chemistry B 1 (2013) 3962-3971.

[15] M. Chang, E. Stride, M. Edirisinghe, Controlling the thickness of hollow polymeric microspheres prepared by electrohydrodynamic atomization, Journal of the Royal Society Interface 7 (2010) S451-S460.

[16] C. Zhang, M. Chang, Y. Li, Y. Qi, J. Wu, Z. Ahmad, J. Li, Janus particle synthesis via aligned non-concentric angular nozzles and electrohydrodynamic co-flow for tunable drug release, RSC advances 6 (2016) 77174-77178.
[17] M. Chang, E. Stride, M. Edirisinghe, A new method for the preparation of monoporous hollow microspheres, Langmuir 26 (2010) 5115-5121.
[18] C. Zhang, C. Gao, M. Chang, Z. Ahmad, J. Li, Continuous micron-scaled rope engineering using a rotating multi-nozzle electrospinning emitter, Applied Physics Letters 109 (2016) 151903.
[19] B. Wang, X. Chen, Z. Ahmad, J. Huang, M.-W. Chang, 3D electrohydrodynamic printing of highly aligned dual-core graphene composite matrices, Carbon 153 (2019) 285-297.
[20] Z. Ahmad, H. Zhang, U. Farook, M. Edirisinghe, E. Stride, P. Colombo, Generation of multilayered structures for biomedical applications using a novel tri-needle coaxial device and electrohydrodynamic flow, Journal of the Royal Society Interface 5 (2008) 1255-1261.
[21] S. Labbaf, H. Ghanbar, E. Stride, M. Edirisinghe, Preparation of multilayered polymeric structures using a novel four-needle coaxial electrohydrodynamic device, Macromolecular rapid communications 35 (2014) 618-623.
[22] L. Cao, J. Luo, KehuaTu, L.-Q. Wang, H. Jiang, Generation of nano-sized core–shell particles using a coaxial tri-capillary electrospray-template removal method, Colloids and Surfaces B: Biointerfaces 115 (2014) 212-218.
[23] C. Zhang, Y. Li, Y. Hu, Y. Peng, Z. Ahmad, J. Li, M. Chang, Porous Yolk–Shell Particle Engineering via Nonsolvent-Assisted Trineedle Coaxial Electrospraying for Burn-Related Wound Healing, ACS applied materials & interfaces 11 (2019) 7823-7835.
[24] Z. Yao, C. Zhang, Z. Ahmad, Y. Peng, M. Chang, Microparticle formation via tri-needle coaxial electrospray at stable jetting modes, ACS Industrial & Engineering Chemistry Research 59 (2020) 14423-14432.
[25] Y. Gao, D. Zhao, M.-W. Chang, Z. Ahmad, J.-S. Li, Optimising the shell thickness-to-radius ratio for the fabrication of oil-encapsulated polymeric microspheres, Chemical Engineering Journal 284 (2016) 963-971.
[26] H. Lee, S. An, S. Kim, B. Jeon, M. Kim, I.S. Kim, Readily Functionalizable and Stabilizable Polymeric Particles with Controlled Size and Morphology by Electrospray, Scientific Reports 8 (2018) 15725.
[27] Y. Gao, M.-W. Chang, Z. Ahmad, J.-S. Li, Magnetic-responsive microparticles with customized porosity for drug delivery, Rsc Advances 6 (2016) 88157-88167.
[28] Z.-C. Yao, Y. Gao, M.-W. Chang, Z. Ahmad, J.-S. Li, Regulating poly-caprolactone fiber characteristics in-situ during one-step coaxial electrospinning via enveloping liquids, Materials Letters 183 (2016) 202-206.
[29] Z. Xing, C. Zhang, C. Zhao, Z. Ahmad, J.-S. Li, M.-W. Chang, Targeting oxidative stress using tri-needle electrospray engineered Ganoderma lucidum polysaccharide-loaded porous yolk-shell particles, European Journal of Pharmaceutical Sciences 125 (2018) 64-73.
[30] L.-F. Zhu, J.-S. Li, J. Mai, M.-W. Chang, Ultrasound-assisted synthesis of chitosan from fungal precursors for biomedical applications, Chemical Engineering Journal 357 (2019) 498-507.
[31] M. Taylor, A.J. Urquhart, M. Zelzer, M.C. Davies, M.R. Alexander, Picoliter water contact angle measurement on polymers, Langmuir 23 (2007) 6875-6878.
[32] Z.C. Yao, S.C. Chen, Z. Ahmad, J. Huang, M.W. Chang, J.S. Li, Essential oil bioactive fibrous membranes prepared via coaxial electrospinning, Journal of food

science 82 (2017) 1412-1422.
[33] Z.-C. Yao, J.-C. Wang, Z. Ahmad, J.-S. Li, M.-W. Chang, Fabrication of patterned three-dimensional micron scaled core-sheath architectures for drug patches, Materials Science and Engineering: C 97 (2019) 776-783.
[34] Z.-C. Yao, J.-C. Wang, B. Wang, Z. Ahmad, J.-S. Li, M.-W. Chang, A novel approach for tailored medicines: Direct writing of Janus fibers, Journal of Drug Delivery Science and Technology 50 (2019) 372-379.
[35] N.A. Peppas, J.J. Sahlin, A simple equation for the description of solute release. III. Coupling of diffusion and relaxation, International journal of pharmaceutics 57 (1989) 169-172.
[36] L.-F. Zhu, Z.-C. Yao, Z. Ahmad, J.-S. Li, M.-W. Chang, Synthesis and Evaluation of Herbal Chitosan from Ganoderma Lucidum Spore Powder for Biomedical Applications, Scientific reports 8 (2018) 14608.
[37] C. Zhang, Z.-C. Yao, Q. Ding, J.J. Choi, Z. Ahmad, M.-W. Chang, J.-S. Li, Tri-needle coaxial electrospray engineering of magnetic polymer yolk–shell particles possessing dual-imaging modality, multiagent compartments, and trigger release potential, ACS applied materials & interfaces 9 (2017) 21485-21495.
[38] S.D. Kulkarni, B. Metzger, J.F. Morris, Particle-pressure-induced self-filtration in concentrated suspensions, Physical Review E 82 (2010) 010402.
[39] R. Scardovelli, S. Zaleski, Direct numerical simulation of free-surface and interfacial flow, Annual review of fluid mechanics 31 (1999) 567-603.
[40] S. Wu, Z. Ahmad, J.-S. Li, M.-W. Chang, Fabrication of flexible composite drug films via foldable linkages using electrohydrodynamic printing, Materials Science and Engineering: C 108 (2020) 110393.
[41] C. Zhang, Y. Li, Y. Hu, Y. Peng, Z. Ahmad, J.-S. Li, M.-W. Chang, Porous Yolk–Shell Particle Engineering via Nonsolvent-Assisted Trineedle Coaxial Electrospraying for Burn-Related Wound Healing, ACS applied materials & interfaces 11 (2019) 7823-7835.
[42] J. Lasio, A.M. Allgeier, C.D. Chan, J.D. Londono, E. Najafi, F.J. Woerner, Control of Mechanical Stability of Hollow Silica Particles, and Its Measurement by Mercury Intrusion Porosimetry, Langmuir 33 (2017) 4666-4674.
[43] L.-F. Zhu, X. Chen, Z. Ahmad, J.-S. Li, M.-W. Chang, Engineering of Ganoderma lucidum polysaccharide loaded polyvinyl alcohol nanofibers for biopharmaceutical delivery, Journal of Drug Delivery Science and Technology 50 (2019) 208-216.
[44] G.L. Jadav, V.K. Aswal, H. Bhatt, J.C. Chaudhari, P.S. Singh, Influence of film thickness on the structure and properties of PDMS membrane, Journal of membrane science 415 (2012) 624-634.
[45] J. Wu, N. Wang, L. Wang, H. Dong, Y. Zhao, L. Jiang, Unidirectional water-penetration composite fibrous film via electrospinning, Soft Matter 8 (2012) 5996-5999.
[46] H. Lee, H. Hwang, Y. Kim, H. Jeon, G. Kim, Physical and bioactive properties of multi-layered PCL/silica composite scaffolds for bone tissue regeneration, Chemical Engineering Journal 250 (2014) 399-408.
[47] O. Ishai, L. Cohen, Elastic properties of filled and porous epoxy composites, International Journal of Mechanical Sciences 9 (1967) 539-546.
[48] S. Balivada, R.S. Rachakatla, H. Wang, T.N. Samarakoon, R.K. Dani, M. Pyle, F.O. Kroh, B. Walker, X. Leaym, O.B. Koper, A/C magnetic hyperthermia of melanoma mediated by iron (0)/iron oxide core/shell magnetic nanoparticles: a mouse study, BMC cancer 10 (2010) 119.
[49] S. Whitaker, The method of volume averaging, Springer Science & Business Media 13 (2013).

[50] B.A. Blakeney, A. Tambralli, J.M. Anderson, A. Andukuri, D.-J. Lim, D.R. Dean, H.-W. Jun, Cell infiltration and growth in a low density, uncompressed three-dimensional electrospun nanofibrous scaffold, Biomaterials 32 (2011) 1583-1590.
[51] B. Wang, Z. Ahmad, J. Huang, J.-s. Li, M.-W. Chang, Development of random and ordered composite fiber hybrid technologies for controlled release functions, Chemical Engineering Journal 343 (2018) 379-389.
[52] Y. Zhang, Y.-T. Wu, W. Zheng, X.-X. Han, Y.-H. Jiang, Pei-LinHu, Z.-X. Tang, L.-E. Shia, The antibacterial activity and antibacterial mechanism of a polysaccharide from Cordyceps cicadae, Journal of Functional Foods 38 (2017) 273-279.
[53] S. Park, H.-h. Kim, S.B. Yang, J.-H. Moon, H.-W. Ahn, J. Hong, A Polysaccharide-Based Antibacterial Coating with Improved Durability for Clear Overlay Appliances, ACS Appl. Mater. Interfaces 10 (2018) 17714–17721.
[54] Z.-C. Yao, L.-J. Jin, Z. Ahmad, J. Huang, M.-W. Chang, J.-S. Li, Ganoderma lucidum polysaccharide loaded sodium alginate micro-particles prepared via electrospraying in controlled deposition environments, International Journal of Pharmaceutics 524 (2017) 148-158.

Figure Captions

Figure 1. (a) A schematic diagram of the tri-needle co-axial jetting system for particle assembly. (b) Diagram elucidating sacrificial agent removal from particles to produce multi-scale porous structure (or films). (c) Particle deposition and coalescence forming the porous structure.

Figure 2. Optical microscope images of porous films obtained via particles deposition before (a, b) and after (c, d) sacrificial agent removal; (e-h) SEM images presenting cross-sections of the composite structure; SEM images showing upper (i, j) and lower (k, l) surface morphology of the structure after sacrificial agent treatment.

Figure 3. Chemical components detection. (a) FTIR spectra of relevant chemicals and the structures before and after templating treatments; (b) XRD spectra of the porous structure and relevant chemicals.

Figure 4. (a) Pore size distribution of the porous structure; (b) Surface water contact angles variation with different deposition thickness of the porous structure; (c) Strain-stress curve of the porous structure.

Figure 5. Magnetism and MRI imaging results. (a) Hysteresis loop of the porous structure, the inserted image presents the structure stained with Prussian-blue; (b) samples embedded in agar gels for MRI imaging; Gray-scale maps of T_1 (c) and T_2 (d) weighting MRI imaging of porous structure with different macro-scale structures, pictures in the first row show the cross-section of samples, the bottom row presenting the longitudinal section.

Figure 6. (a) Release profile of the porous structure; (b-d) Upper surface morphology of the structure after 120 h release, where (c) and (d) are the magnified images of (b); (e-g) Lower surface morphology of the structure after 120 h release, where (f) and (g) are the magnified images of (e).

Figure 7. Fluorescent images showing cell distribution on the upper and lower surfaces of the structures at different culture time periods, scale bar: 200 μm.

Figure 8. Fluorescent micrographs showing cell migration on petri dish and upper surface on the porous structure post 3-day culture, with a 30° tilting angle during the incubation. The nuclei was stained with DAPI (blue) and cytoskeleton stained with rhodamine-phalloidin (red). Merged images are shown in the right column, scale bar:

200 μm; the second and fourth lines are the magnified scope of the first and third line, respectively, with a field of 200 μm×200 μm.

Figure 9. (a) Stereoscopic distribution of cells in 2D (on the petri dish) and 3D (on the porous structures) culture at different time points; (b) At different culture periods, the projection of the maximum fluorescence intensity at xy, yz, and xz orientations, with cytoskeletal being stained in red, nucleus in blue. Scale bar: 100 μm.

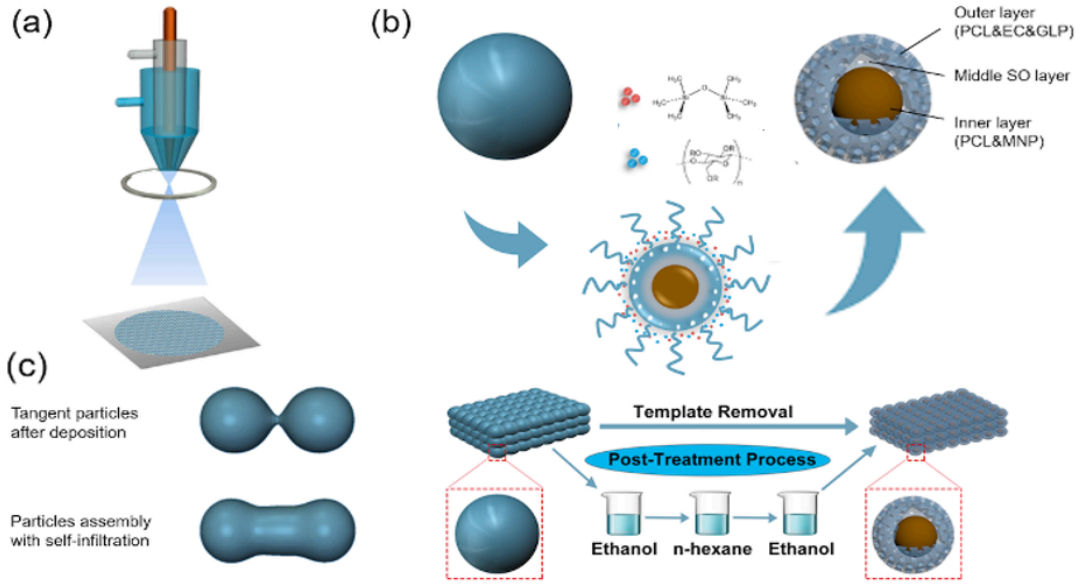
(a)
(b)
Outer layer
(PCL&EC&GLP)
Middle SO layer
Inner layer
(PCL&MNP)
(c)
Tangent particles
after deposition
Particles assembly
with self-infiltration
Template Removal
Post-Treatment Process
Ethanol
n-hexane
Ethanol

Figure 1.

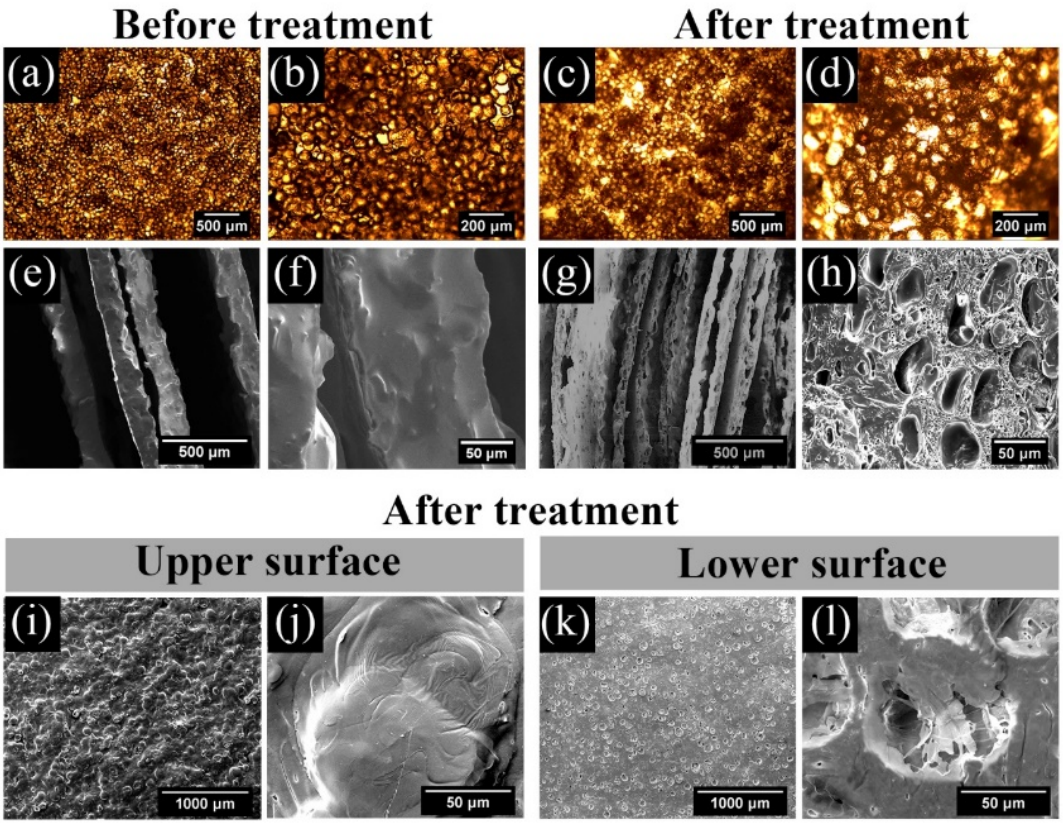
Before treatment
After treatment
(a)
(b)
(c)
(d)
500 µm
200 µm
500 µm
200 µm
(e)
(f)
(g)
(h)
500 µm
50 µm
500 µm
50 µm
After treatment
Upper surface
Lower surface
(i)
(j)
(k)
(l)
1000 µm
50 µm
1000 µm
50 µm

Figure 2.

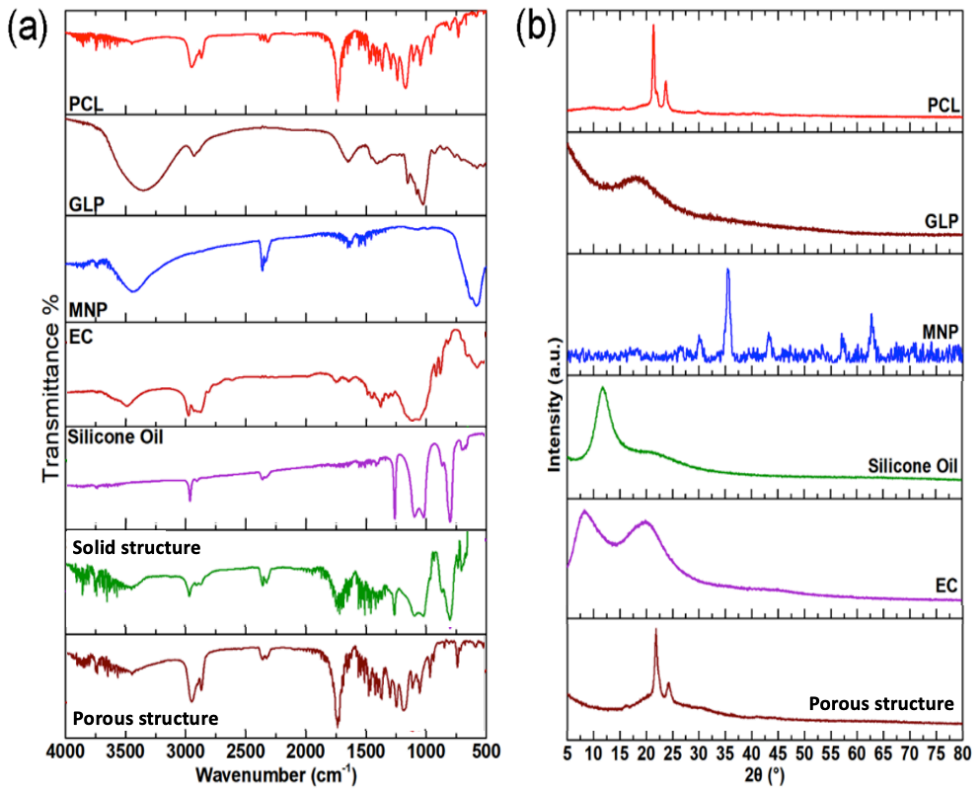
(a)
PCL
GLP
MNP
EC
Silicone Oil
Solid structure
Porous structure
Transmittance %
4000 3500 3000 2500 2000 1500 1000 500
Wavenumber (cm-1)
(b)
PCL
GLP
MNP
Silicone Oil
EC
Porous structure
Intensity (a.u.)
5 10 15 20 25 30 35 40 45 50 55 60 65 70 75 80
2θ (°)

Figure 3.

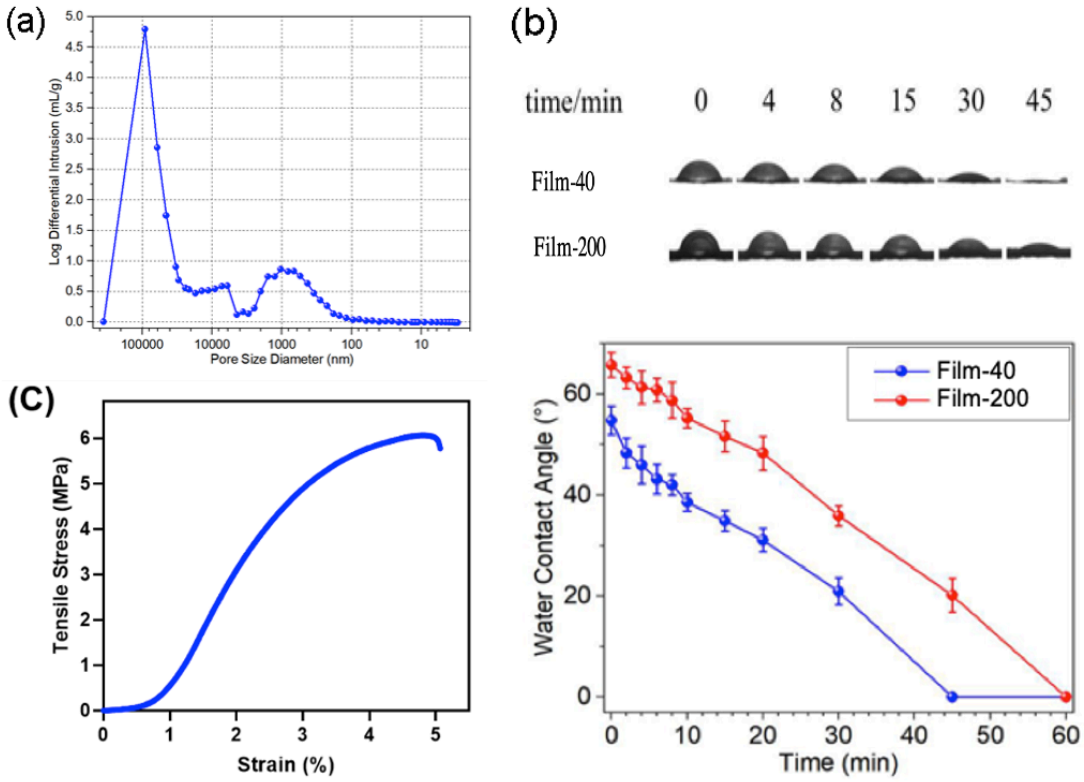
(a)
Log Differential Intrusion (mL/g)
Pore Size Diameter (nm)
100000
10000
1000
100
10
(b)
time/min
0
4
8
15
30
45
Film-40
Film-200
(C)
Tensile Stress (MPa)
Strain (%)
Water Contact Angle (°)
Time (min)
Film-40
Film-200

Figure 4.

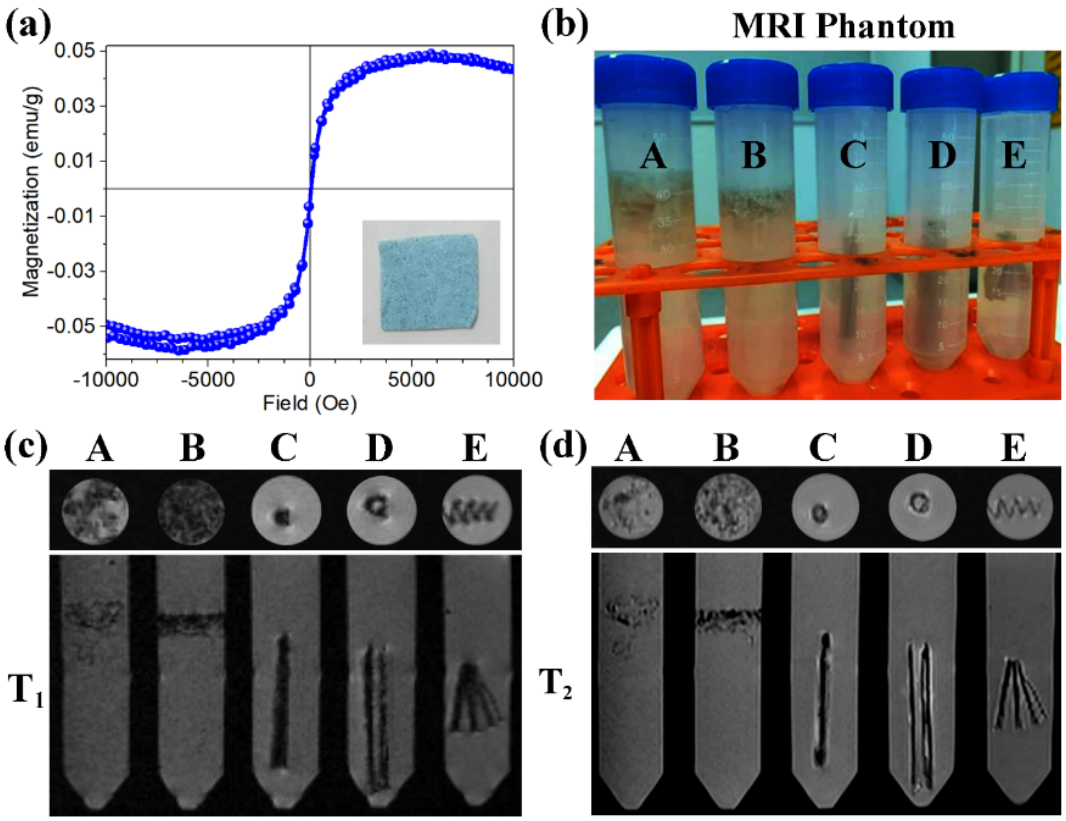
(a)
Magnetization (emu/g)
0.05
0.03
0.01
-0.01
-0.03
-0.05
-10000
-5000
0
5000
10000
Field (Oe)
(b)
MRI Phantom
A
B
C
D
E
(c)
A
B
C
D
E
T1
(d)
A
B
C
D
E
T2

Figure 5.

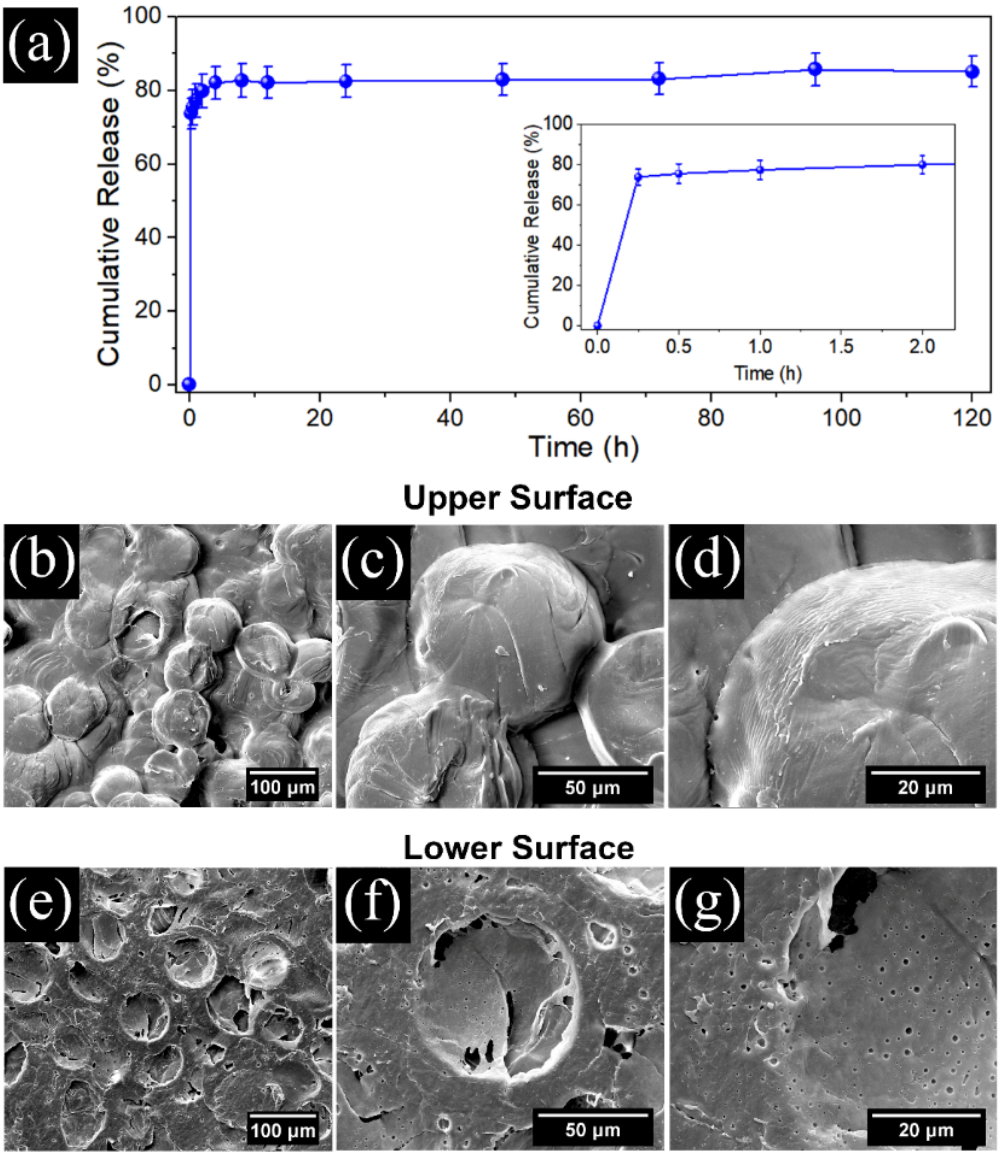
(a)
Cumulative Release (%)
Time (h)
Upper Surface
(b)
(c)
(d)
100 μm
50 μm
20 μm
Lower Surface
(e)
(f)
(g)
100 μm
50 μm
20 μm

Figure 6.

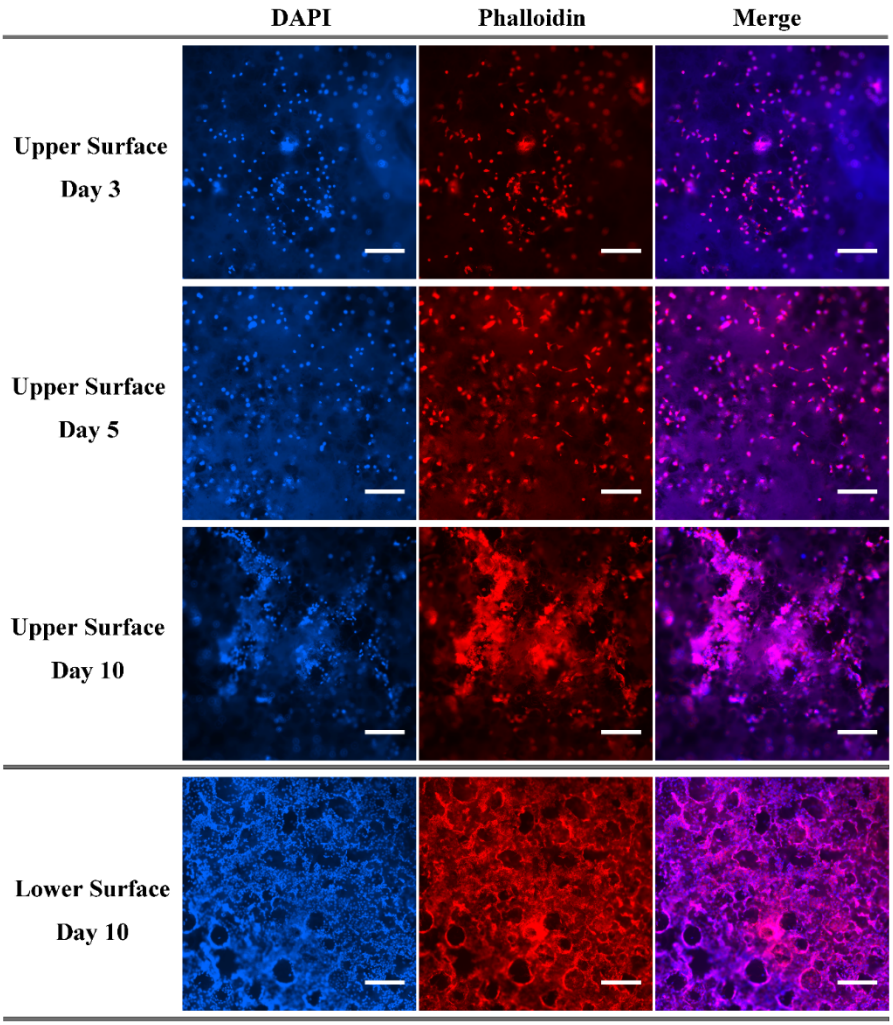
DAPI
Phalloidin
Merge
Upper Surface
Day 3
Upper Surface
Day 5
Upper Surface
Day 10
Lower Surface
Day 10

Figure 7.

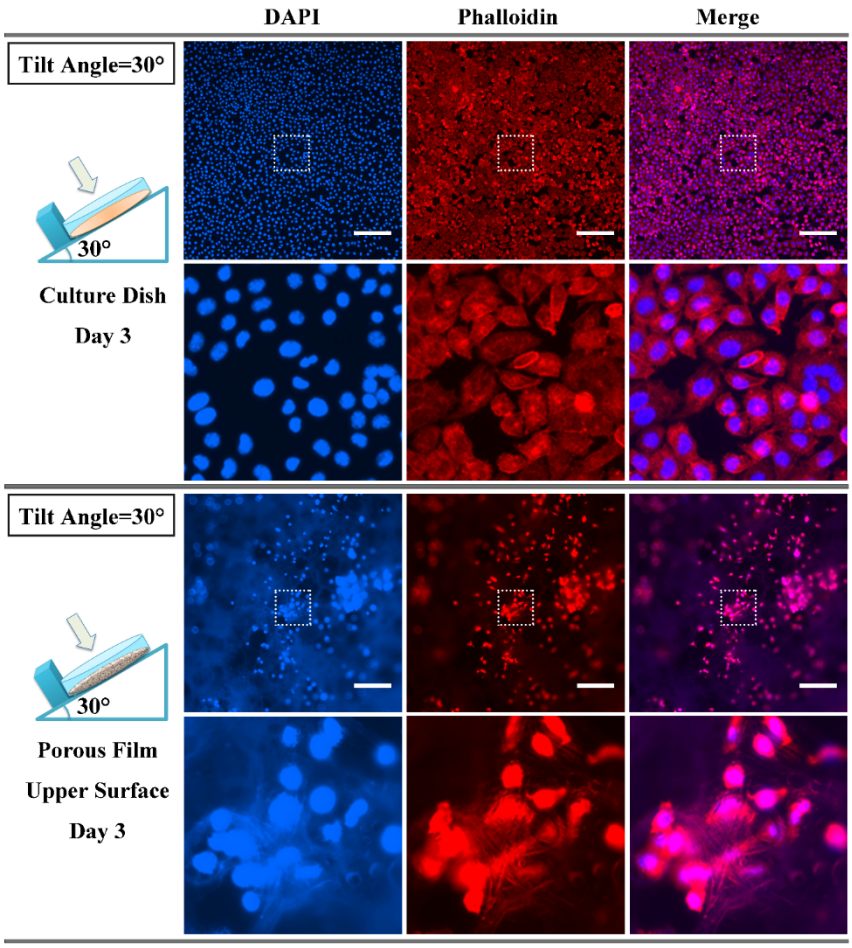
DAPI
Phalloidin
Merge
Tilt Angle=30°
30°
Culture Dish
Day 3
Tilt Angle=30°
30°
Porous Film
Upper Surface
Day 3

Figure 8.

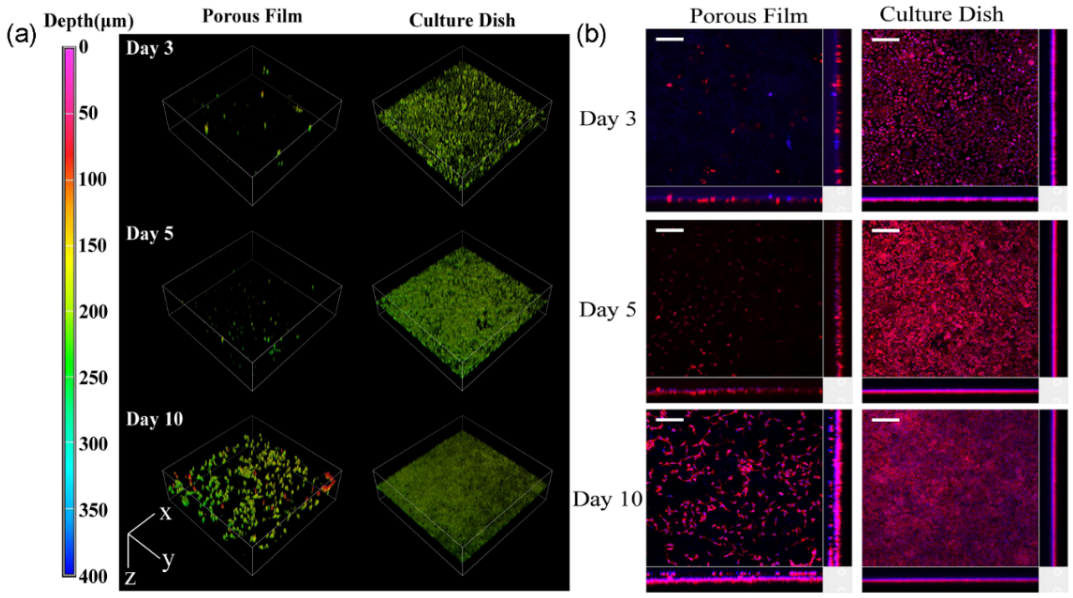
(a)
Depth(μm)
0
50
100
150
200
250
300
350
400
Porous Film
Culture Dish
Day 3
Day 5
Day 10
x
y
z
(b)
Porous Film
Culture Dish
Day 3
Day 5
Day 10

Figure 9.